RSC Advances

PAPER

View Article Online
View Journal | View Issue

Cite this: *RSC Adv.*, 2025, **15**, 40698

Fluorescence sensing of glucose at nanomolar levels using an imprinted copolymer embedded with carbon quantum dots

Dinh Khoi Dang,[a] Vo Thi Kim Xuyen,[a] Qui Thanh Hoai Ta*[b] and Ly Tan Nhiem*[a]

Received 3rd August 2025
Accepted 17th October 2025

DOI: 10.1039/d5ra05656j

rsc.li/rsc-advances

Monitoring glucose levels in intracellular fluid is important in healthcare, as it directly correlates with cell metabolism-related diseases. However, conventional methods typically require high-end equipment and can only be performed in laboratory settings. In this study, an imprinted copolymer composed of 3-aminopropyltriethoxysilane and tetraethyl orthosilicate, embedded with carbon quantum dots (CQDs), was developed for fluorescence-based glucose sensing. A facile preparation method yielded CQDs with sizes ranging from 0.7 to 5 nm and fluorescence emission at a wavelength of 435 nm. These CQDs were incorporated into a polymeric matrix in the presence of glucose, followed by a molecular imprinting process. The resulting polymeric particles exhibited a diameter of approximately 604 ± 15 nm and contained binding cavities that matched the spatial arrangement of hydroxyl groups on glucose. The fluorescence intensity of the CQDs was highly dependent on glucose adsorption. Leveraging these properties, the imprinted polymer exhibited successful glucose recognition in the intracellular fluid-mimicking solution, achieving a limit of detection of 29.4 nM. A good linear correlation ($R^2 = 0.9884$) was observed between the logarithmic glucose concentration (25 nM to 25 mM) and changes in fluorescence intensity. This fluorescent sensor demonstrates significant potential for real-world applications in monitoring intracellular glucose levels.

Introduction

Recently, monitoring intracellular glucose levels has played a vital role in studying cellular glucose uptake,[1,2] providing insights into cancer metabolism,[3,4] diabetes-related cellular dysfunction,[5] and neurodegenerative diseases.[6] This often requires sensors capable of detecting nanomolar concentrations of glucose, typically 100 nM to 10 μM.[5,6] Additionally, tear and sweat fluids contain glucose at concentrations that correlate with blood glucose levels but are significantly lower[7–9] (~0.1–1 mM *vs.* 3.9–5.5 mM in blood), making them promising non-invasive alternatives for blood glucose monitoring. However, sub-micromolar glucose monitoring heavily relies on conventional techniques such as mass spectrometry including LC-MS and GC-MS,[10–12] which offer high accuracy but are high cost and time-consuming. While nuclear magnetic resonance spectroscopy addresses some of these limitations, it remains a laboratory-based technique that requires sample pre-purification to achieve adequate sensitivity.[13,14] Several alternative methods have been explored beyond these conventional techniques, including optical-based sensors such as surface-enhanced Raman spectroscopy,[15] surface plasmon resonance,[16,17] and fluorescence sensors.[18] Additionally, electrochemical sensors based on glucose oxidase (GOx)/glucose dehydrogenase (GDH) or nanomaterials (*e.g.*, MoS_2, graphene, metal oxides) have also been developed as recognition elements. However, these methods do not provide the exquisite sensitivity required for nanomolar glucose detection and often exhibit limited selectivity, especially when distinguishing glucose from other common cellular components.

Molecularly imprinted polymers (MIPs), a class of synthetic polymeric materials with tailored recognition sites, have shown promise as ideal molecular recognition layers for glucose detection.[19–21] MIPs possess a high density of binding cavities that are deliberately designed to selectively capture the target analyte. These superior characteristics have been leveraged in various advanced sensing applications, including toxic gas sensors,[22,23] colorimetric detection of aquatic analytes,[19,24] and disease biomarker detection.[18,25] Recently, MIPs have been incorporated with nanostructured materials to enhance sensitivity and selectivity.[20,26] Among these, carbon quantum dots (CQDs) have emerged as promising candidates for integration into sensing platforms. CQDs consist of sp^2-hybridized carbon atoms, which aggregate into clusters of varying sizes and shapes.[27,28] These sp^2 clusters emit light at different

---

[a] *Faculty of Chemical and Food Technology, Ho Chi Minh City University of Technology and Education, 01 Vo Van Ngan Street, Thu Duc Ward, Ho Chi Minh City, Vietnam*

[b] *Institute of Advanced Technology, Vietnam Academy of Science and Technology, 1B TL29 Street, An Phu Dong Ward, Ho Chi Minh City, 700000, Vietnam*

wavelengths when excited by an appropriate incident light source, and the emission intensity is highly dependent on the nature of the clusters and their surrounding environment.[29] Consequently, even a minor environmental change can induce significant variations in the emission spectrum of CQDs.[18,29] Notably, CQDs with an abundance of oxygen-containing functional groups (*e.g.*, carboxyl, carbonyl) exhibit excellent dispersion in aqueous solutions, making them highly compatible with water-dispersible polymers.[29–31] Considering these properties, embedding CQDs within an MIP matrix is expected to create a hybrid sensing structure for glucose detection, where MIPs act as capturing elements, and CQDs serve as transducing elements by modulating fluorescence emission intensity.

In this study, CQDs were embedded into a copolymer matrix prepared from 3-aminopropyltriethoxysilane (APTES) and tetraethoxysilane (TEOS) in the presence of glucose, followed by an imprinting process to create glucose-imprinted polymers. The MIPs doped with CQDs exhibited blue-light emission, which varied depending on the density of glucose molecules bound within the binding cavities. As a result, the imprinted polymer successfully detected glucose at concentrations as low as 2.5 nM.

Experimental

Materials

Tetraethyl orthosilicate (TEOS, 98%), 3-aminopropyltriethoxysilane (APTES, 99%) were purchased from ThermoFisher. Anhydrous acetic acid (CH_3COOH, 99%), ammonium hydroxide (NH_4OH, 30%) were obtained from Merck. Citric acid ($C_6H_8O_7$, 99.5%), Tris hydrochloride (Tris–HCl, 99%), methanol (CH_3OH, 99.9%) and PBS buffer were obtained from Sigma-Aldrich. Potassium chloride (KCl, 99%), calcium chloride ($CaCl_2$, 99%), ammonium chloride (NH_4Cl, 99%), sodium sulfate (Na_2SO_4, 99%), urea (CH_4N_2O, 99%), disodium phosphate dodecahydrate ($Na_2HPO_4\cdot 12H_2O$, 99%), monosodium phosphate dihydrate ($NaH_2PO_4\cdot 2H_2O$), magnesium sulfate heptahydrate ($MgSO_4\cdot 7H_2O$, 99%), and trisodium citrate dehydrate ($C_6H_5Na_3O_7\cdot 2H_2O$, 99%) were purchased from Xilong. Human serum ($\leq$10 EU per mL endotoxin) was obtained from Sigma-Aldrich. De-ionized (DI) water was used in all experiments.

Synthesis of carbon quantum dots and imprinted polymers

2 g of citric acid was annealed at 200 °C using an oil bath. After specific time intervals, the obtained black solid was immersed in 50 mL of Tris–HCl (0.05 M, pH 7.0), followed by sonication for 1 hour. The dispersion was then filtered using a 0.22 μm nylon membrane, and the filtrate was collected, denoted as CQDs, and stored at 5 °C for later use. For the preparation of imprinted polymers incorporated with CQDs, 15 mL of the as-prepared CQDs, 5 mL of DI H_2O, and 60 mg of glucose were mixed under stirring at room temperature for 30 minutes. Then, 30 mL of ethanol was added, and the mixture was heated to 60 °C. Subsequently, 103 μL of acetic acid was added, followed by the addition of 117 μL of APTES, and stirring was continued for 1 hour. Then, 2 mL of TEOS was added, and stirring was continued for an additional 3 hours. The precipitates were collected by centrifugation at 9000 RPM, using water and ethanol as washing solvents. The final product was denoted as CQDs@MIP_glucose. To create binding cavities in the polymer, CQDs@MIP_glucose underwent an extraction process using a Soxhlet apparatus, where a mixture of acetic acid/methanol (v/v 1 : 9) was used as the washing solvent. The reflux boiling process was carried out for 12 hours at 80 °C. The product was thoroughly washed with water and ethanol, then dried at 45 °C, and denoted as CQDs@MIP. For comparison, non-imprinted polymers (NIPs) were fabricated using the same procedure as described above but without the presence of glucose. The resulting product was denoted as CQDs@NIP.

Detection of glucose using CQDs@MIP

100 mg of CQDs@MIP was dispersed in 100 mL of Tris–HCl using sonication for 2 hours, followed by vortexing for 5 minutes. The solution was then diluted twice with PBS buffer (pH = 7), resulting in a stock solution. Separately, a glucose solution was prepared at different concentrations in PBS buffer, ranging from 5 nM to 0.1 M. For the glucose detection, 3 mL of the stock solution was mixed with 3 mL of each glucose solution, followed by vortexing every 5 minutes. After 1 hour, the mixtures underwent mild sonication before being transferred to a quartz cuvette for PL measurement.

Characterization

X-ray photoelectron spectroscopy (XPS, PHI 5000 Versaprobe II) with an energy source of 187 eV was used to investigate the chemical states of CQDs@MIP. X-ray diffraction (XRD, D2 Phaser, Bruker) with a copper X-ray source at 30 kV and 10 mA was employed to study the crystallographic structure of the as-prepared materials. UV-Vis absorbance was measured using UV-Vis spectroscopy (UH 5300, Hitachi), and UV-Vis diffuse reflectance spectroscopy (UV-Vis DRS) was conducted to analyze the bandgap of the CQDs in the wavelength range of 250–800 nm. Fourier-transform infrared spectroscopy (FTIR, Alpha-E, Bruker) was used to analyze the chemical structures in the 450–4000 cm^{-1} range. Transmission electron microscopy (TEM, JEM-1010, Jeol) at 120 kV was used to examine the morphology of the imprinted polymers, while scanning electron microscopy (SEM, JMS-IT 200, Jeol) operated at 10 kV was utilized to study the size and shape. The size distribution was determined using dynamic light scattering (DLS, Zetasizer Pro, Malvern). Photoluminescence spectroscopy (PL, FluoroMax Plus-C Horiba) was applied to induce excitation and measure fluorescence for the CQDs and CQDs@MIP.

Results and discussion

The as-prepared CQDs synthesized at different time intervals were first excited using an excitation wavelength of 360 nm. All the CQDs exhibited corresponding fluorescence spectra with broad emission bands, as shown in Fig. 1. Notably, the CQDs prepared with 30 minutes of annealing showed the highest

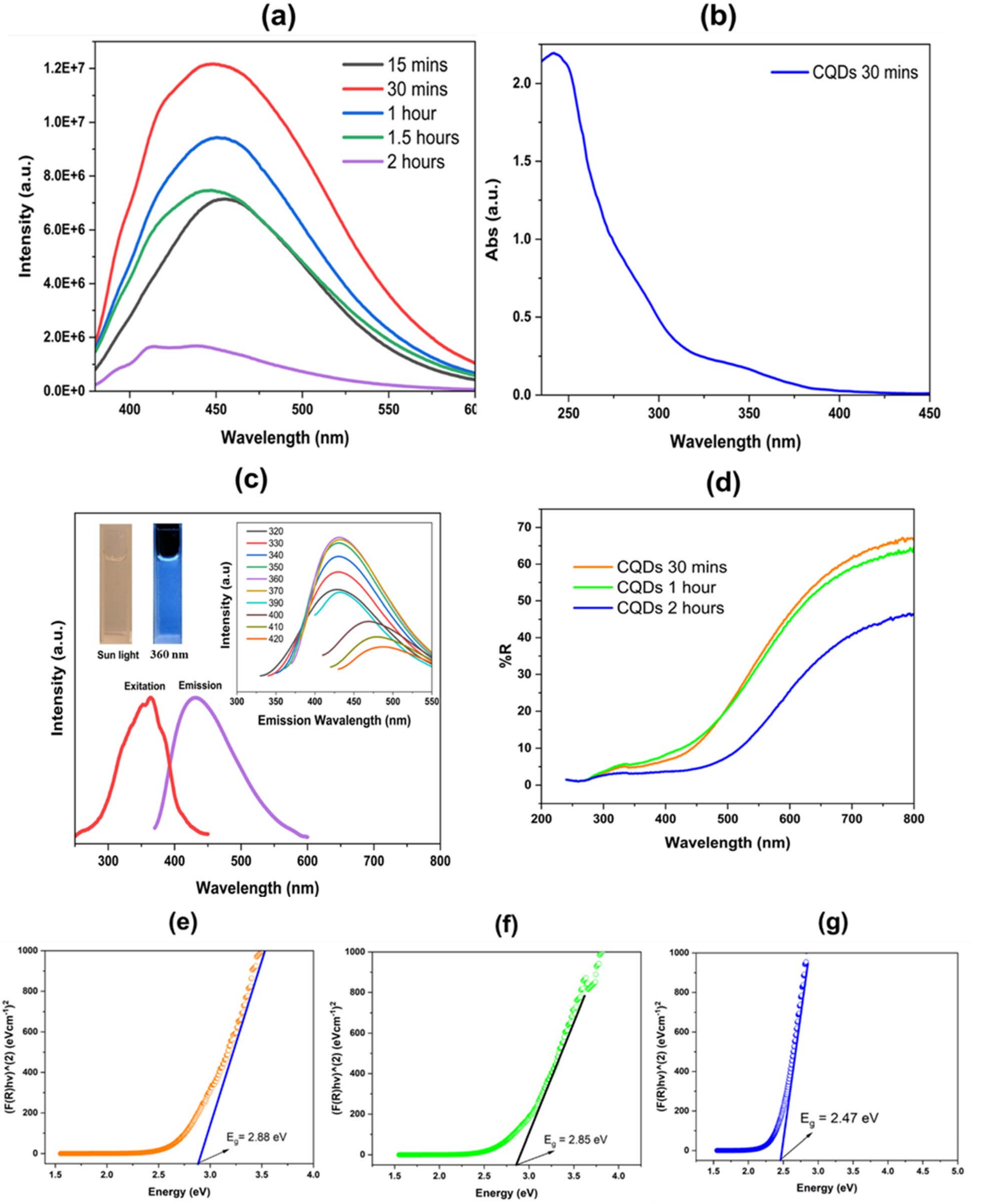

Fig. 1 (a) Fluorescence spectra of CQDs synthesized at different time intervals with an excitation wavelength of 360 nm; (b) UV-Vis absorbance spectrum of CQDs synthesized for 30 minutes; (c) fluorescence spectra of CQDs under different excitation wavelengths; (d) UV-Vis reflectance spectrum of the CQDs; Tauc plots derived from the Kubelka–Munk method for bandgap estimation of CQDs synthesized for (e) 30 minutes, (f) 1 hour, and (g) 2 hours.

fluorescence intensity, with emission ranging from blue to green (400–550 nm) (Fig. 1a). The CQDs were further investigated using UV-Vis absorbance spectroscopy (Fig. 1b). The results showed a peak located at 242 nm, which is characteristic of the $\pi \rightarrow \pi^*$ electronic transition of C=C bonds in the conjugated carbon structure.[32] This transition is commonly observed in aromatic domains or sp^2-hybridized carbon networks, indicating the presence of graphitic or polyaromatic structures within the CQDs.[33,34] Furthermore, a transition plateau was observed from 320 nm to 360 nm, attributed to the $n \rightarrow \pi^*$ transition of C═O bonds.[35] The CQDs were also exposed to a range of excitation wavelengths, from 320 nm to 420 nm (Fig. 1c). Excitation at 360 nm produced the highest emission spectrum, with a peak at 435 nm. At longer excitation wavelengths, weaker fluorescence emission was observed. To explain these results, the DRS was analyzed (Fig. 1d), followed by bandgap calculations using the Kubelka–Munk method.[36,37] The bandgap values were determined to be 2.88, 2.84, and 2.47 eV for annealing times of 30 minutes, 1 hour, and 2 hours, respectively, as shown in Fig. 1e–g. It is known that longer annealing times produce larger CQDs, which results in smaller corresponding bandgaps, and *vice versa*.[29,38] Consequently, smaller CQDs tend to be effectively excited by shorter wavelengths to emit light, while larger CQDs require longer wavelengths to reach excited states. This helps explain the fluorescence emissions as observed above. The CQDs prepared for 30 minutes were selected for incorporation into the MIP, as described above. As shown in Fig. 2, the FTIR spectrum of the CQDs showed an absorption band at 1723 cm^{-1}, which corresponds to the vibrational mode of the carbonyl (C═O) group.[39,40] Broad bands in the range of 3000 to 3700 cm^{-1} were attributed to the stretching vibrations of hydroxyl (O–H) groups,[41] and a distinct signal at 1167 cm^{-1} was assigned to C–O stretching.[42] These signals were significantly reduced in the spectra of CQDs@NIP, CQDs@MIP_glucose, and CQDs@MIP, indicating the successful incorporation of the CQDs into the polymer matrix. Instead, characteristic absorption bands of the copolymer structure appeared.[43,44] These included a peak at 1540 cm^{-1}, attributed to N–H bending and C–N stretching vibrations, as well as peaks at 1072 and 1120 cm^{-1}, assigned to the asymmetric stretching of Si–O–Si and Si–O–C bonds, respectively. Additionally, a peak at 793 cm^{-1} was observed, which corresponds to the symmetric stretching mode of the Si–O–Si framework.[45]

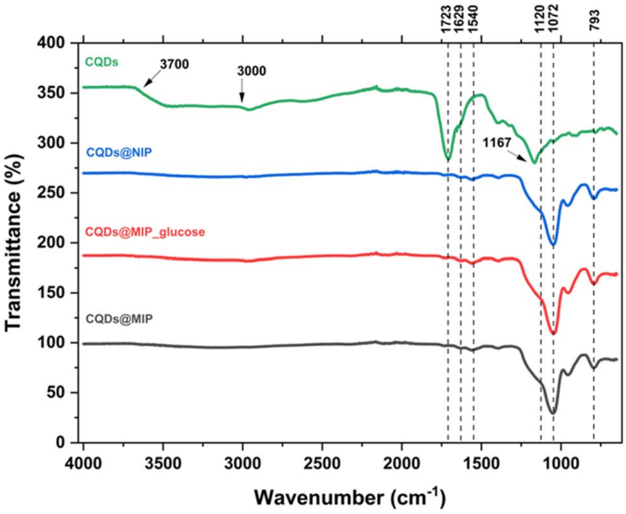

Fig. 2 FTIR spectra of the as-prepared materials including CQDs, CQDs@NIP, CQDs@MIP_glucose and CQDs@MIP.

The chemical states of CQDs@MIP were further confirmed using XPS spectra, as shown in Fig. 3. In the Si 2p orbital,

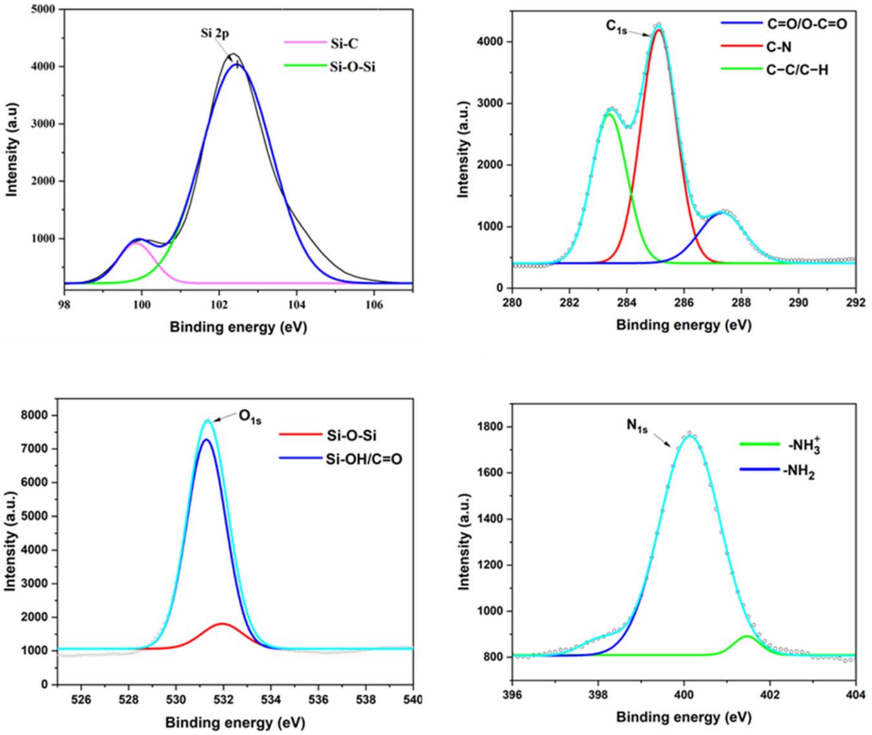

Fig. 3 XPS spectra of the CQDs@MIP, showing Si 2p, C 1s, O 1s and N 1s orbitals.

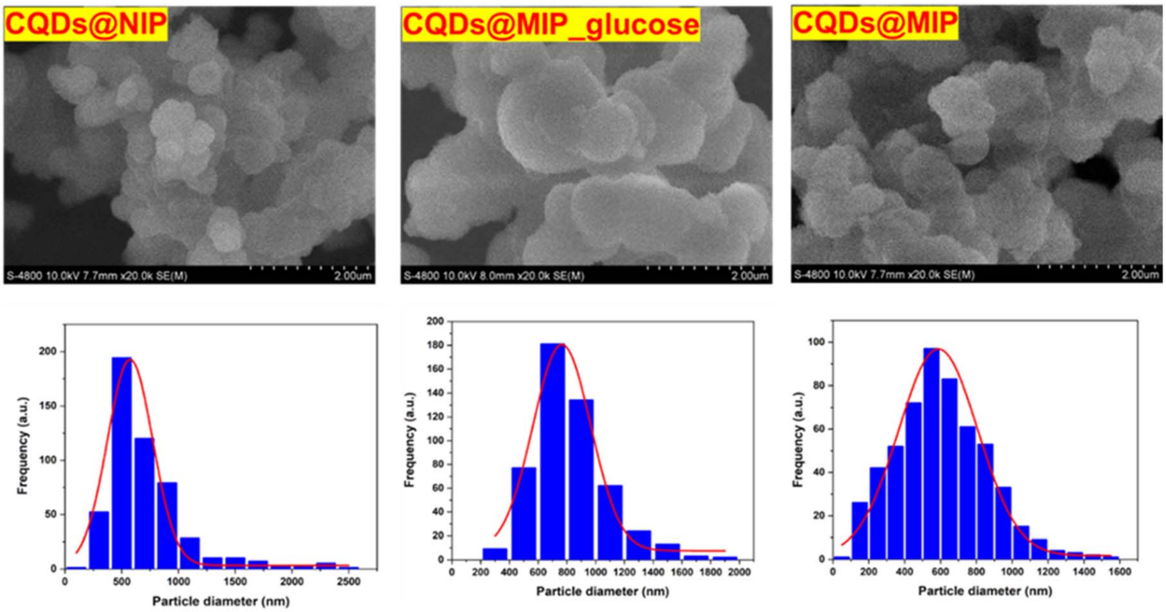

Fig. 4 SEM images and corresponding particle size distributions of CQDs@NIP, CQDs@MIP_glucose, and CQDs@MIP.

a dominant peak was observed at a binding energy (BE) of 102.5 eV, corresponding to Si–O–Si bonds,[46,47] indicating successful condensation between APTES and TEOS. Additionally, a small portion of Si–C bonds remained in the copolymers, characterized by a peak at BE = 99.8 eV.[48] In the C 1s orbital, a characteristic peak for C–N bonds appeared at BE = 285.2 eV, originating from the bonding of amine groups with carbon in APTES molecules and from Tris–HCl used during the preparation of CQDs.[49,50] Furthermore, C═O and O–C═O bonds were located at BE = 287.4 eV, confirming the presence of CQDs in the polymer matrix,[39] consistent with the UV-Vis absorbance results discussed above. Peaks at BE = 531.1 eV and BE = 400.5 eV, corresponding to Si–OH/C═O and $-NH_2$ groups,[47,49] respectively, provide additional confirmation of the desired chemical states in the resulting MIPs. The morphology and size of the MIPs were revealed by SEM images, as shown in Fig. 4. The size distributions of CQDs@NIP, CQDs@MIP_glucose, and CQDs@MIP were determined to be 707 ± 19 nm, 823 ± 16 nm, and 604 ± 15 nm, respectively. All the as-prepared materials exhibited quasi-spherical particles, indicating the successful formation of copolymers, as described previously. It can be observed that CQDs@MIP_glucose particles are significantly larger than those of CQDs@NIP. This increase in size can be attributed to the presence of glucose template molecules, which have a high affinity for the amine groups in the APTES molecules *via* hydrogen bonding. This interaction leads to the formation of complexes and a concomitant increase in particle size.[44,51] After template extraction, a significant reduction in particle size was observed for CQDs@MIP. This extraction step is crucial in the preparation of imprinted polymers, as it removes the embedded glucose molecules from the polymer matrix, resulting in the formation of binding cavities with

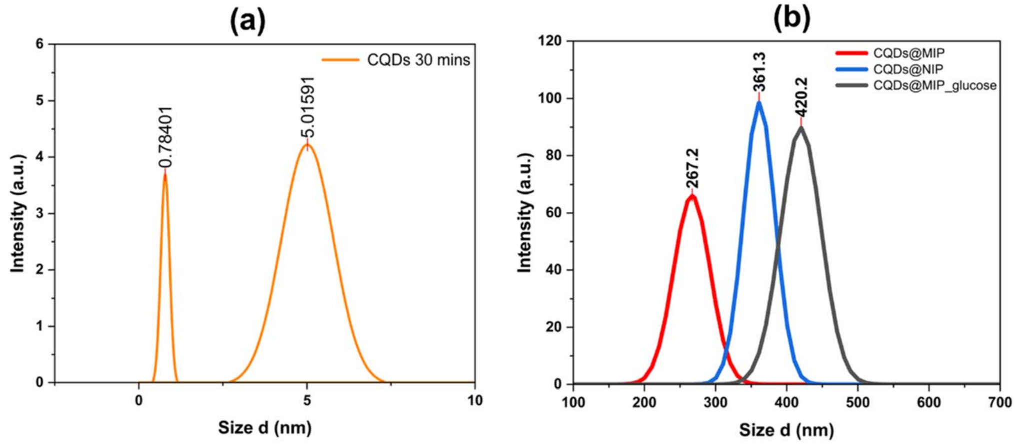

Fig. 5 DLS spectra showing the particle size distributions of (a) CQDs, and (b) CQDs@NIP, CQDs@MIP_glucose, and CQDs@MIP.

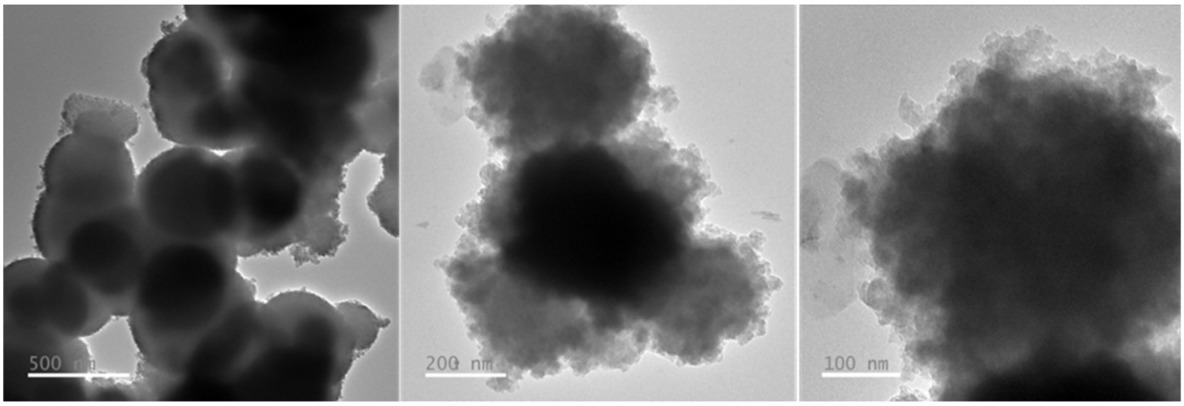

Fig. 6 TEM images of CQDs@MIP at different magnifications with scale bars of 500 nm, 200 nm, and 100 nm.

dimensions and functionalities complementary to glucose.[25] Dynamic size distribution was also analyzed using DLS (Fig. 5). The dynamic size of the CQDs was found to range from 0.7 nm to 5 nm, which is a typical size range for CQDs prepared by this annealing method.[32] Interestingly, the MIPs exhibited dynamic sizes in the same trend as observed in the SEM results, with sizes of 361 nm, 420 nm, and 267 nm for CQDs@NIP, CQDs@MIP_glucose, and CQDs@MIP, respectively.

To further investigate the morphology of CQDs@MIP, TEM analysis was conducted, as shown in Fig. 6. At various magnifications, CQDs@MIP appeared as quasi-spherical particles. Notably, the edges of the particles were diffuse, indicating a loosely cross-linked surface layer. The irregular and soft edges may result from the imprinting process, which can produce a less compact outer structure. Such edge features are characteristic of MIPs synthesized with template molecules, where surface porosity and flexibility are desirable for effective target binding.[44,52] At this point, the morphology and chemical structures of the as-prepared MIPs have been elucidated, as described above. The CQDs were shown to be embedded within the imprinted copolymers of APTES-TEOS. The interaction between CQDs and APTES is mainly achieved through the hydrolysis of the ethoxy groups of APTES into silanol groups,[53] which subsequently undergo condensation with the hydroxyl or carboxyl groups present on the CQDs surface.[54,55] This process results in the formation of covalent Si–O–C linkages, providing a stable anchoring of APTES on CQDs. In addition, hydrogen bonding and electrostatic interactions between protonated amine groups ($-NH_3^+$) of APTES and negatively charged functional groups (–COOH/–OH) on CQDs further enhance the surface modification.

Utilizing the fluorescence emission of the CQDs, the sensing principle is illustrated in Fig. 7. The polymeric layers, also embedded with the template glucose, act as shielding barriers that significantly reduce the fluorescence of the CQDs by blocking both the incident and emitted light. After template removal, resulting in the formation of binding cavities, the shielding effect diminishes, leading to a concomitant increase in fluorescence intensity. In other words, the presence of the template glucose strongly influences the fluorescence emission intensity of the CQDs when excited. Based on this mechanism, when glucose is adsorbed onto the CQDs@MIP, the binding cavities become occupied. As the glucose concentration in the solution increases, more cavities are filled, enhancing the

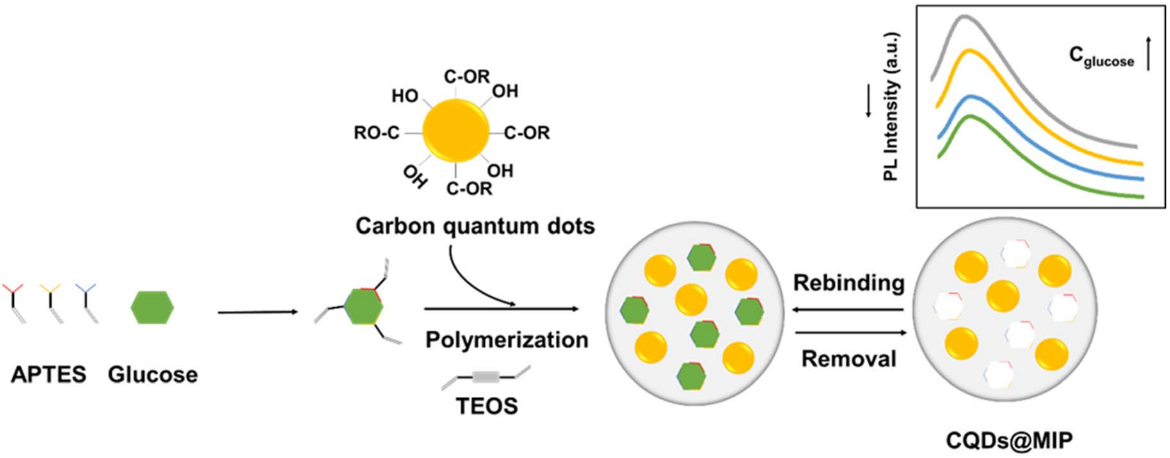

Fig. 7 Schematic illustration of the fabrication process and sensing mechanism of CQDs@MIP.

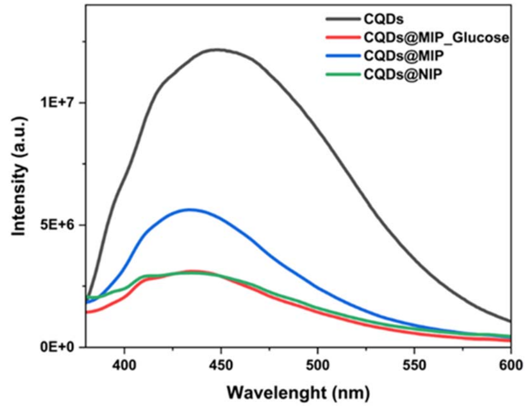

Fig. 8 Fluorescence spectra of the as-prepared materials under an excitation wavelength of 360 nm.

shielding effect and thereby decreasing the fluorescence intensity. As a result, the fluorescence spectra of the as-prepared materials are shown in Fig. 8. The CQDs exhibited a fluorescence spectrum with a peak at 435 nm and an intensity of approximately $F = 1.2 \times 10^7$. Following incorporation into the copolymers, both CQDs@NIP and CQDs@MIP_glucose exhibited a marked decrease in fluorescence intensity, with F measured at 3×10^6 (a.u.). However, upon template removal to generate binding cavities in CQDs@MIP, the fluorescence intensity increased to $F = 5.6 \times 10^6$ (a.u.). These trends are consistent with the sensing mechanism discussed above.

As shown in Fig. S1, the CQDs@MIP prepared with polymerization times of 3 and 4 hours exhibited the highest fluorescence intensity, and a polymerization time of 3 hours was selected for the subsequent preparation of CQDs@MIP. The effect of pH on the fluorescence intensity was also investigated (Fig. S2), demonstrating that a neutral pH of 7.0 is most suitable for the CQDs@MIP.

The CQDs@MIP was then employed to adsorb glucose from buffer solutions at varying concentrations, ranging from 2.5 nM to 0.05 M. As depicted in Fig. 9a, higher glucose concentrations resulted in lower fluorescence intensities, a trend governed by the sensing mechanism discussed above. The relationship between glucose concentration and the normalized fluorescence signal was established, as shown in Fig. 9b, where F_0 and F represent the maximum fluorescence intensities of CQDs@MIP without and with glucose adsorption, respectively. At glucose concentrations of 2.5 nM and 1 mM, the F_0/F ratios were 1.73 (a.u.) and 1.99 (a.u.), respectively. Beyond a concentration of 1 mM, further increases led to progressively smaller changes in fluorescence intensity, indicating saturation of the adsorption sites. Interestingly, the CQDs@NIP was also immersed in glucose solutions across the same concentration range, followed by fluorescence measurements. It was observed that the fluorescence intensities exhibited changes upon glucose immersion, but the magnitudes were much lower compared to those observed with CQDs@MIP. The F_0/F ratios were distinguishable across the different glucose concentrations, measuring 1.47 (a.u.) and 1.52 (a.u.) at 2.5 nM and 1 mM, respectively. These results strongly suggest that glucose molecules were capable of binding to the non-imprinted polymers. However, these bindings were non-specific, occurring mainly on the outer layer of the CQDs@NIP through hydrogen bonding between glucose molecules and abundant hydroxyl groups on the copolymers, rather than within the specific binding cavities created during the imprinting process.[44,51,52] This non-specific interaction resulted in rapid adsorption saturation, as observed. Overall, these results further emphasize the critical role of binding cavities in the selective binding of glucose.

As shown in Fig. 10, the F_0/F ratio of the CQDs@MIP upon exposure to the interfering molecules ranged from 1.25 (a.u.) to 1.48 (a.u.), which was much lower compared to that observed with glucose. This indicates that the interfering molecules adsorbed on the CQDs@MIP, resulting in a reduction of fluorescence intensity. However, these bindings can be attributed to non-specific interactions at the outer layer of the MIP, rather than the occupation of the imprinted binding cavities by the

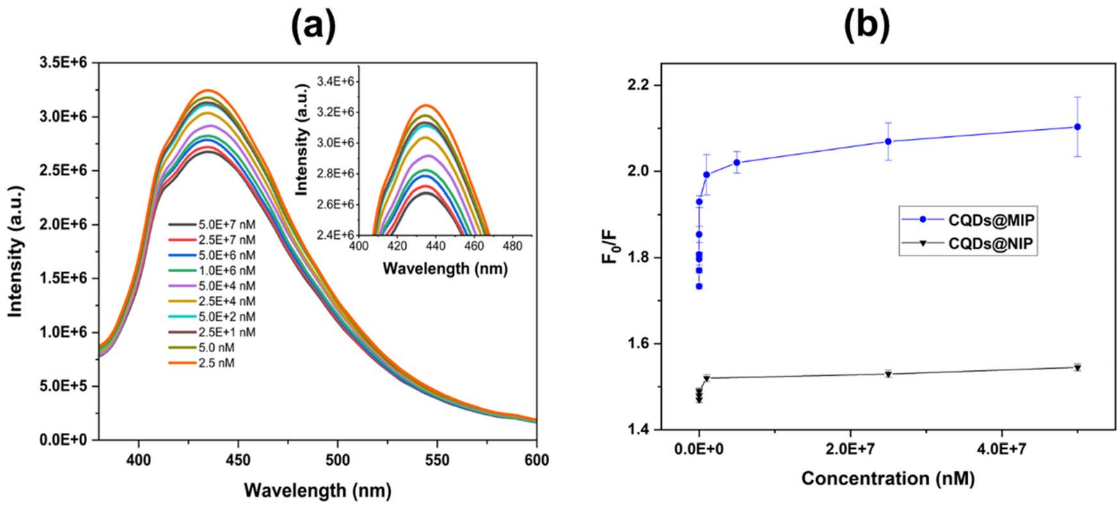

Fig. 9 (a) Fluorescence spectra of CQDs@MIP after glucose adsorption at various concentrations, (b) relationship between glucose concentration and the fluorescence intensity ratio (F_0/F) for CQDs@MIP and CQDs@NIP. The adsorption experiments were performed in PBS buffer.

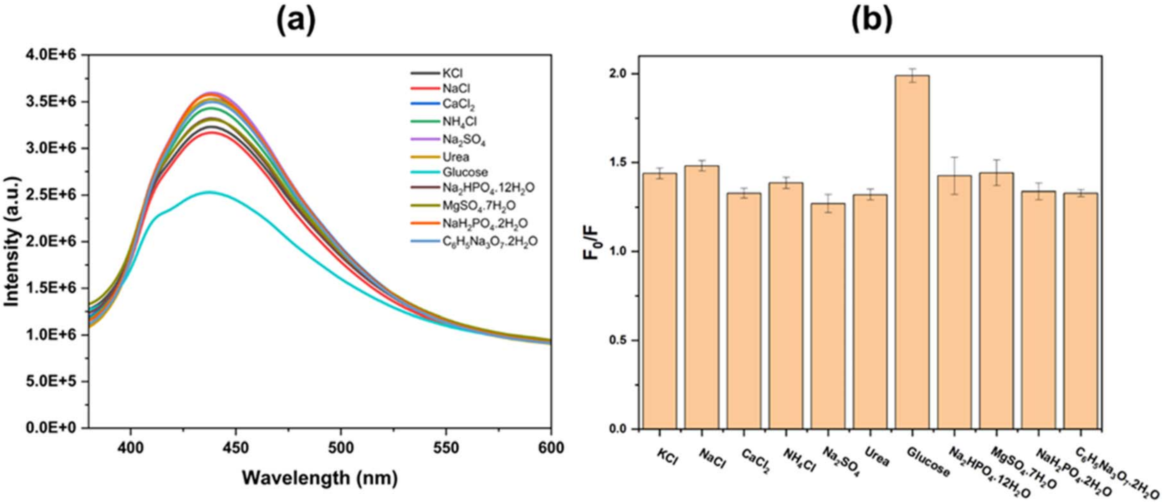

Fig. 10 CQDs@MIP after adsorption of different analytes at a concentration of 1 mM: (a) fluorescence spectra and (b) corresponding fluorescence intensity ratio (F_0/F).

analytes. The high specificity of the imprinted polymer toward glucose can be attributed to several synergistic factors. First, the imprinted binding cavities possess a three-dimensional geometry that is complementary in size and shape to the glucose molecule, thereby restricting access of non-target molecules with different steric profiles.[25,51] Second, the spatial arrangement of hydrogen-bonding sites within the cavities closely matches the distribution of hydroxyl groups in glucose,

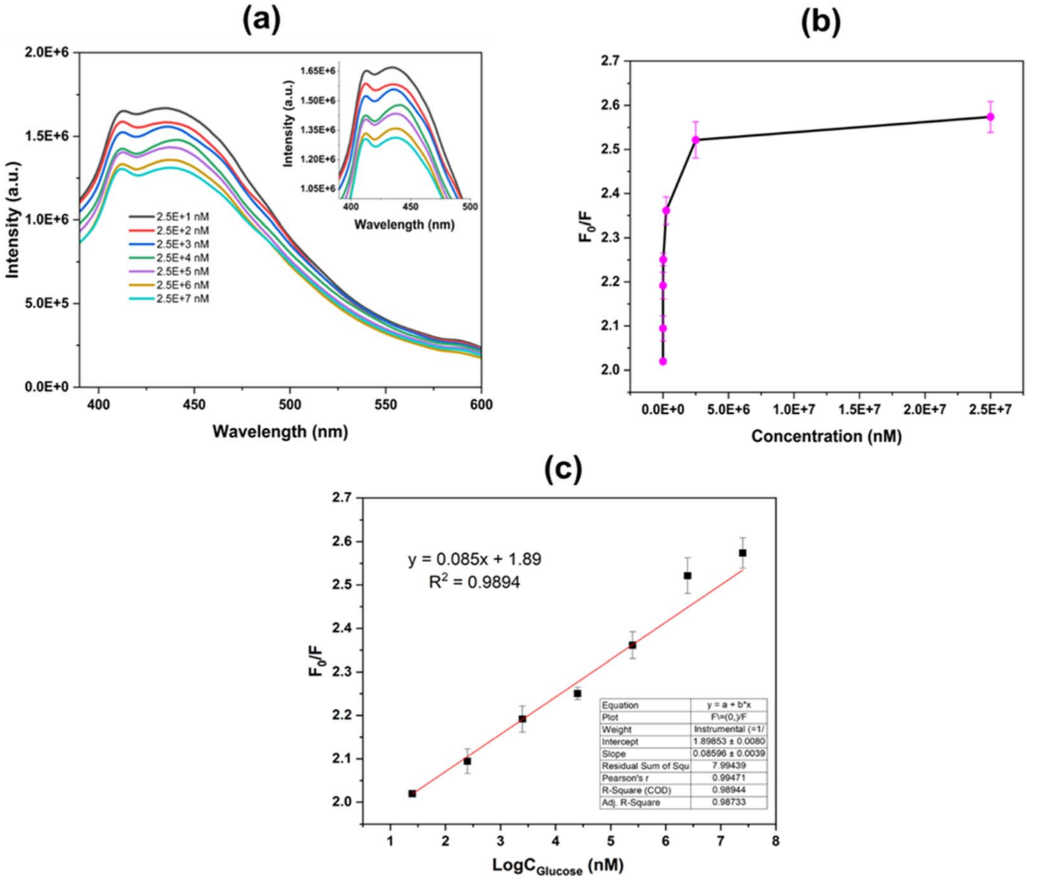

Fig. 11 (a) Fluorescence spectra of CQDs@MIP after glucose adsorption at various concentrations, ranging from 25 nM to 25 mM, in an intracellular fluid-mimicking solution. (b) Corresponding relationship between glucose concentration and fluorescence intensity ratio (F_0/F). (c) Logarithmic relationship between glucose concentration and fluorescence intensity ratio (F_0/F).

Table 1 Comparison of glucose detection using different approaches

Approach/material	Transduction method	LOD	Year	References
Fe_3O_4-based MIP	Colorimetric	10 μM, in serum	2025	57
TCS3200 RGB sensor	Colorimetric	0.9–3.9 mg dL^{-1}, in saliva	2025	60
MIP + LC-MS/MS	Chromatographic	0.30 ng mL^{-1}, in fish serum	2024	61
Core-shell structures	Luminescence	0.03 μM, in serum	2024	62
CQDs/MIP	Fluorescence	29.1 nM, in intracellular-mimicking fluid	2025	This work

allowing for multiple simultaneous interactions that strengthen recognition.[56,57] Therefore, the exclusion effect arising from mismatched molecular dimensions and functional group orientation further minimizes non-specific adsorption, ensuring a high degree of selectivity. Collectively, these features endow the glucose-imprinted polymer with a superior molecular recognition capability compared to its non-imprinted counterpart. To provide further evidence, zeta potential measurements and Raman spectral analyses were included in the SI (Fig. S3 and S4), both of which confirm the presence of hydrogen-bonding interactions between glucose and the polymer matrix.

Based on these results, a further assessment was conducted. An intracellular fluid-mimicking solution was prepared by diluting the interfering molecules into human serum at the concentrations listed in Table S1. Glucose was then added at varying concentrations ranging from 25 nM to 25 mM. The CQDs@MIP were immersed into these solutions, and the resulting fluorescence spectra were recorded, as shown in Fig. 11. Although the fluorescence intensities were lower compared to those in DI water, each CQDs@MIP exposed to different glucose concentrations produced distinguishable fluorescence spectra and corresponding changes in the F_0/F ratios, measuring 2.02 (a.u.) at 25 nM and 2.57 (a.u.) at 0.25 mM. Within this concentration range, the F_0/F ratio exhibited a linear relationship with glucose concentration, while saturation behavior was observed at glucose concentrations above 2.5 mM. This exponential response is consistent with the Beer–Lambert law.[58,59] Accordingly, a logarithmic relationship between glucose concentration and the F_0/F ratio was established as follows: $F_0/F = 0.085\log(C_{\text{glucose}}) + 1.89$, with $R^2 = 0.9884$. As demonstrated, the as-prepared CQDs@MIP was capable of detecting glucose in a intracellular fluid-mimicking environment in the presence of various interfering molecules. The limit of detection (LOD) was determined to be 29.4 nM (SI), which is relevant to intracellular glucose levels and can be applied for direct glucose monitoring.[1,10] The simplicity and high selectivity of this fluorescence sensor highlight its potential as an alternative to conventional high-end techniques.

In comparison with other studies as shown in Table 1, Nhiem *et al.* reported glucose detection using a colorimetric transduction approach based on MIPs, achieving a detection limit as low as 10 μM in aqueous solution,[57] which is significantly higher than the LOD obtained in the current study. In another MIPs-based approach, salivary glucose levels in diabetic patients were monitored with low LODs ranging from 0.9 mg dL^{-1} to 3.9 mg dL^{-1} using 3,3′,5,5′-tetramethylbenzidine as the color indicator.[60] Additionally, when MIPs were combined with liquid chromatography-tandem mass spectrometry, glucose in fish serum was detected with an LOD of 0.30 ng mL^{-1}.[61] However, the requirement for mass spectrometry limits the widespread applicability of this method. Furthermore, a core–shell structure of upconversion nanoparticles was employed for glucose detection in serum samples, achieving an LOD of 0.03 μM, based on single-band bright red luminescence.[62] To the best of our knowledge, no previous studies have reported the use of MIPs combined with fluorescence transduction to achieve a nanomolar-level LOD as demonstrated in the present work.

Conclusions

In this study, APTES and TEOS were used to prepare a copolymer in the presence of CQDs, which were previously synthesized *via* a facile annealing process of citric acid. The resulting copolymer underwent a washing step to produce an imprinted polymer embedded with binding cavities, referred to as CQDs@MIP. The imprinted polymer exhibited a quasi-spherical shape with an average diameter of approximately 604 ± 15 nm and showed a high degree of structural disorder at the edges. The CQDs@MIP demonstrated high performance in detecting glucose in an intracellular fluid-mimicking solution, with a LOD of 29.4 nM, yielding an F_0/F ratio of 2.02 (a.u.), which is relevant to physiological intracellular glucose levels. Within the glucose concentration range of 25 nM to 25 mM, a logarithmic relationship was established: $F_0/F = 0.085\log(C_{\text{glucose}}) + 1.89$, with $R^2 = 0.9884$. These findings demonstrate the high potential of this sensing approach for practical applications in intracellular glucose monitoring.

Author contributions

Dinh Khoi Dang: conceptualization, methodology, initial draft preparation; Vo Thi Kim Xuyen: investigation, data curation; Qui Thanh Hoai Ta: sample preparation, formal analysis, initial draft preparation and final editing; Ly Tan Nhiem: conceptualization, supervision, writing – review & editing, funding acquisition, project administration.

Conflicts of interest

There are no conflicts to declare.

Data availability

The data supporting this article have been included as part of the supplementary information (SI). See DOI: https://doi.org/10.1039/d5ra05656j.

Acknowledgements

The authors gratefully acknowledge the financial support from Ho Chi Minh City University of Technology and Education under its 2025 research funding program as reference number of T2025-98.

References

1 A. Behjousiar, C. Kontoravdi and K. M. Polizzi, *PLoS One*, 2012, **7**, e34512.
2 B.-H. Hou, H. Takanaga, G. Grossmann, L.-Q. Chen, X.-Q. Qu, A. M. Jones, S. Lalonde, O. Schweissgut, W. Wiechert and W. B. Frommer, *Nat. Protoc.*, 2011, **6**, 1818–1833.
3 L. W. S. Finley, *Cell*, 2023, **186**, 1670–1688.
4 R. J. DeBerardinis and N. S. Chandel, *Sci. Adv.*, 2016, **2**, e1600200.
5 A. Fijany, L. R. Sayadi, N. Khoshab, D. A. Banyard, A. Shaterian, M. Alexander, J. R. T. Lakey, K. Z. Paydar, G. R. D. Evans and A. D. Widgerow, *Mol. Biol. Rep.*, 2019, **46**, 1459–1475.
6 B. L. Tang, *J. Cell. Physiol.*, 2020, **235**, 7653–7662.
7 J. T. Baca, D. N. Finegold and S. A. Asher, *The Ocular Surface*, 2007, **5**, 280–293.
8 J. R. Sempionatto, L. C. Brazaca, L. García-Carmona, G. Bolat, A. S. Campbell, A. Martin, G. Tang, R. Shah, R. K. Mishra, J. Kim, V. Zucolotto, A. Escarpa and J. Wang, *Biosens. Bioelectron.*, 2019, **137**, 161–170.
9 S. R. Corrie, J. W. Coffey, J. Islam, K. A. Markey and M. a. F. Kendall, *Analyst*, 2015, **140**, 4350–4364.
10 M. Wang, J. Xu, N. Yang, T. Zhang, H. Zhu and J. Wang, *Front. Endocrinol.*, 2022, **12**, 807318.
11 B. Luo, K. Groenke, R. Takors, C. Wandrey and M. Oldiges, *J. Chromatogr. A*, 2007, **1147**, 153–164.
12 K. R. Reid, C. F. Burant and R. T. Kennedy, *Anal. Chem.*, 2009, **81**, 9201.
13 D. E. Befroy and G. I. Shulman, *Diabetes*, 2011, **60**, 1361–1369.
14 J. H. F. Bothwell and J. L. Griffin, *Biol. Rev.*, 2011, **86**, 493–510.
15 X. Sun, *Anal. Chim. Acta*, 2022, **1206**, 339226.
16 W. Zheng, B. Han, S. E, Y. Sun, X. Li, Y. Cai and Y. Zhang, *Microchem. J.*, 2020, **157**, 105010.
17 B. Karki, A. Jha, A. Pal and V. Srivastava, *Opt. Quantum Electron.*, 2022, **54**, 595.
18 H.-C. Wang and A.-R. Lee, *J. Food Drug Anal.*, 2015, **23**, 191–200.
19 L. T. Nhiem, C. H. Q. Quy, H. N. A. Tuan, M. H. Do, J.-S. Noh and Q. T. H. Ta, *Microchem. J.*, 2025, **208**, 112347.
20 L. Chen, X. Wang, W. Lu, X. Wu and J. Li, *Chem. Soc. Rev.*, 2016, **45**, 2137–2211.
21 R. Zhang, S. Xu, Y. Zhu, W. Zhao, J. Luo, X. Liu and D. Tang, *Biosens. Bioelectron.*, 2016, **85**, 381–386.
22 P. Azhdary, S. Janfaza, S. Fardindoost, N. Tasnim and M. Hoorfar, *Anal. Chim. Acta*, 2023, **1278**, 341749.
23 Y. Zhang, J. Zhang and Q. Liu, *Sensors*, 2017, **17**, 1567.
24 L. Thi Mong Thy, B. Hoang Nhan and L. T. Nhiem, *ACS Appl. Nano Mater.*, 2024, **7**, 14964–14971.
25 G. Selvolini and G. Marrazza, *Sensors*, 2017, **17**, 718.
26 J. J. BelBruno, *Chem. Rev.*, 2019, **119**, 94–119.
27 G. Eda, Y.-Y. Lin, C. Mattevi, H. Yamaguchi, H.-A. Chen, I.-S. Chen, C.-W. Chen and M. Chhowalla, *Adv. Mater.*, 2010, **22**, 505–509.
28 P. Tian, L. Tang, K. S. Teng and S. P. Lau, *Mater. Today Chem.*, 2018, **10**, 221–258.
29 S. Ying Lim, W. Shen and Z. Gao, *Chem. Soc. Rev.*, 2015, **44**, 362–381.
30 L. Tian, Z. Li, P. Wang, X. Zhai, X. Wang and T. Li, *J. Energy Chem.*, 2021, **55**, 279–294.
31 R. Das, R. Bandyopadhyay and P. Pramanik, *Mater. Today Chem.*, 2018, **8**, 96–109.
32 J. Schneider, C. J. Reckmeier, Y. Xiong, M. von Seckendorff, A. S. Susha, P. Kasák and A. L. Rogach, *J. Phys. Chem. C*, 2017, **121**, 2014–2022.
33 S. Bhattacharyya, *Carbon Superstructures: From Quantum Transport to Quantum Computation*, CRC Press, 2024.
34 F. F. Sead, Y. Jadeja, A. Kumar, M. M. Rekha, M. Kundlas, S. Saini, K. Kant Joshi and H. Noorizadeh, *Nanoscale Adv.*, 2025, **7**, 3961–3998.
35 L. Cao, M. J. Meziani, S. Sahu and Y.-P. Sun, *Acc. Chem. Res.*, 2013, **46**, 171–180.
36 P. Makuła, M. Pacia and W. Macyk, *J. Phys. Chem. Lett.*, 2018, **9**, 6814–6817.
37 S. Landi, I. R. Segundo, E. Freitas, M. Vasilevskiy, J. Carneiro and C. J. Tavares, *Solid State Commun.*, 2022, **341**, 114573.
38 Y. Dong, J. Shao, C. Chen, H. Li, R. Wang, Y. Chi, X. Lin and G. Chen, *Carbon*, 2012, **50**, 4738–4743.
39 H. Hou, C. E. Banks, M. Jing, Y. Zhang and X. Ji, *Adv. Mater.*, 2015, **27**, 7861–7866.
40 Y. Dong, J. Lin, Y. Chen, F. Fu, Y. Chi and G. Chen, *Nanoscale*, 2014, **6**, 7410–7415.
41 S. Azeez and R. Shenbagaraman, in *Characterization Techniques in Bionanocomposites*, ed. S. Ahmed and C. M. Hussain, Woodhead Publishing, 2025, pp. 209–227.
42 M. Asemani and A. R. Rabbani, *J. Pet. Sci. Eng.*, 2020, **185**, 106618.
43 I. A. Rahman, M. Jafarzadeh and C. S. Sipaut, *Ceram. Int.*, 2009, **35**, 1883–1888.
44 L. Thi Mong Thy, B. Hoang Nhan and L. T. Nhiem, *ACS Appl. Nano Mater.*, 2024, **7**, 14964–14971.
45 P. K. Jal, M. Sudarshan, A. Saha, S. Patel and B. K. Mishra, *Colloids Surf., A*, 2004, **240**, 173–178.
46 M. E. Simonsen, C. Sønderby, Z. Li and E. G. Søgaard, *J. Mater. Sci.*, 2009, **44**, 2079–2088.
47 B. Ulgut and S. Suzer, *J. Phys. Chem. B*, 2003, **107**, 2939–2943.

48 E. A. Dalchiele, A. Aurora, G. Bernardini, F. Cattaruzza, A. Flamini, P. Pallavicini, R. Zanoni and F. Decker, *J. Electroanal. Chem.*, 2005, **579**, 133–142.
49 R. G. Acres, A. V. Ellis, J. Alvino, C. E. Lenahan, D. A. Khodakov, G. F. Metha and G. G. Andersson, *J. Phys. Chem. C*, 2012, **116**, 6289–6297.
50 H. Hafeez, D. Keun Choi, C. Min Lee, P. Justin Jesuraj, D. Hyun Kim, A. Song, K. Bum Chung, M. Song, J. Fei Ma, C.-S. Kim and S. Yoon Ryu, *RSC Adv.*, 2019, **9**, 7536–7542.
51 L. Chen, X. Wang, W. Lu, X. Wu and J. Li, *Chem. Soc. Rev.*, 2016, **45**, 2137–2211.
52 L. T. Nhiem, C. H. Q. Quy, H. N. A. Tuan, M. H. Do, J.-S. Noh and Q. T. H. Ta, *Microchem. J.*, 2025, **208**, 112347.
53 A. Zarinwall, T. Waniek, R. Saadat, U. Braun, H. Sturm and G. Garnweitner, *Langmuir*, 2021, **37**, 171–179.
54 J. Yu, C. Dong, Y. Yang, S. Yu and T. Chen, *Microchem. J.*, 2024, **204**, 110949.
55 A. Majid, Y. Tian, H. Li, L. Tan, R. Haider and J. Wang, *Journal of Water Process Engineering*, 2025, **74**, 107816.
56 J. J. BelBruno, *Chem. Rev.*, 2019, **119**, 94–119.
57 L. T. Nhiem, C. H. Q. Quy, H. N. A. Tuan, M. H. Do, J.-S. Noh and Q. T. H. Ta, *Microchem. J.*, 2025, **208**, 112347.
58 D. F. Swinehart, The Beer-Lambert Law, DOI: 10.1021/ed039p333, accessed May 20, 2025.
59 L. Kocsis, P. Herman and A. Eke, *Phys. Med. Biol.*, 2006, **51**, N91.
60 A. Vaidya, J. Sahoo and P. Shende, *Int. J. Pharm.*, 2025, **671**, 125219.
61 B. Yao, L. Gu, L. Huang, R. Li, Z. Fan, Z. Chen, D. Qin and L. Gao, *Polymers*, 2024, **16**, 1538.
62 T. Zhao, D. Wu, X. Zhang and H. Lyu, *Anal. Chim. Acta*, 2024, **1295**, 342323.